Design and Optimization of a Novel Hydro Cylinder Displacement Sensor

Jie Zhou (zhoujiesxh@foxmail.com)
CCTEG Coal Science and Technology Research Institute https://orcid.org/0000-0002-1682-5029
Zhiguo Wen
CCTEG Coal Science and Technology Research Institute
Huaiwei Ren
CCTEG Coal Science and Technology Research Institute
Zhe Han
CCTEG Coal Science and Technology Research Institute
Shixin Gong
CCTEG Coal Science and Technology Research Institute

Research

Keywords: Displacement Sensor, Adaptive Kalman Filtering, Hydro Cylinder, Coal Mine

Posted Date: April 9th, 2021

DOI: https://doi.org/10.21203/rs.3.rs-403142/v1

Article

Design and Optimization of a Novel Hydro Cylinder Displacement Sensor

Jie Zhou [1, 2, *] and Zhiguo Wen[1, 2], Huaiwei Ren [1, 2], Zhe Han [1, 2], Shixin Gong [1, 2]

[1]*CCTEG Coal Science and Technology Research Institute, Beijing 100013, China*

[2]*Coal Science Research Institute, Mining Research Branch, Beijing 100013, China*

*Correspondence: zhoujiesxh@foxmail.com;

Tel.: +86-1326-058-8121

Received: date; Accepted: date; Published: date

Abstract: In recent years, the coal mine intelligent development process has constantly advanced, putting forward higher requirements for monitoring mining equipment data. Sensor technology suitable for the special underground environment has also been developing. Hydraulic support is a key piece of equipment in fully mechanized coal mining. Monitoring the hydraulic support position and attitude has been an important part of coal mine intelligent development. In the present paper, a new oil cylinder displacement sensor was proposed. The oil cylinder translational motion was transformed into the magnet rotary motion via the motion conversion mechanism. The magnet angle was calculated by utilizing the single-chip microcomputer, and the oil cylinder expansion and contraction were calculated via the filtering algorithm. Results showed that the sensor accuracy could reach 0.5 mm.

Keywords: *Displacement Sensor; Adaptive Kalman Filtering; Hydro Cylinder; Coal Mine*

1. Introduction

The existing cylinder travel sensor can be divided into the built-in cylinder and the external cylinder travel sensors.

Much research exists considering the external type displacement sensor. According to the principle, the external displacement sensor can be divided into the optical sensor[1-3], hall sensor[4, 5], and eddy current sensor[6-8]. Optic displacement sensors have the advantages of high accuracy and fine resolution, but they are expensive and sensitive to dust and vibration[9]. A hall sensor is relatively less expensive, and it is not as sensitive to dust and oil pollution as an optic sensor, so the hall sensor has been applied thoroughly in the scene with low precision requirements[5, 10, 11]. Furthermore, the eddy sensor is a non-contact

linearization measuring tool that can accurately measure the static and dynamic relative displacement changes between the measured body and the probe end face[7]. However, the coal mine environment is complex and involves many kinds of equipment. These external sensors are easily damaged when utilized underground[12, 13].

The current market share of the oil cylinder travel sensor in the underground coal mine, subject to service conditions, is the displacement sensor[14-16], which utilizes the magnetostrictive principle to generate a strain pulse signal through the intersection of two different magnetic fields to accurately measure their positions. It adopts the non-contact measurement method because the measuring magnetic ring and the sensor have no direct contact, friction, or wear, thereby permitting on the ground long service life, strong environmental adaptability, high reliability, and good safety, which are convenient for the system automation work. However, the complicated downhole environment means that the hydraulic support cannot keep parallel with the moving axis of the sensor in the moving process, and the production process of domestic manufacturers is limited, resulting in the low reliability of the magnetostrictive sensor in the actual use process, as well as the service life not be guaranteed.

In the present paper, a new displacement sensor was proposed to measure the oil cylinder telescopic stroke. The proposed sensor can be fixed with one end of the cylinder, and the rope end is fixed with the cylinder pushrod. The linear motion of the cylinder can be converted into the rotation motion of the output end of the sensor via the sensor motion transformation structure. The cylinder displacement can be calculated by detecting the rotating magnetic field signal at the sensor output. Also, an adaptive Kalman filter algorithm based on particle swarm optimization was proposed to improve the sensor precision.

The present paper was organized as follows: in Section 2, the measurement principle was presented, including the mechanical structure and the data acquisition circuit of the proposed sensor; in Section 3, the method of displacement calculation was introduced and an adaptive Kalman filtering was proposed to improve sensor accuracy; in Section 4, the sensor and the algorithm performances were tested via real experiments. Finally, Section 5 concluded with the findings of the present paper.

2. Design of Absolute Displacement Sensor

2.1. Modified Structure of Proposed Displacement Sensor

Figure 2 shows a schematic illustration of the proposed displacement sensor. As shown, the motion conversion part was comprised of three fixed pulleys, a rotating wheel, a shaft, a bevel gear, and a worm. When the hydro cylinder was extending and contracting, it pulled the string to move along a straight line, and one end of the string was fixed with the hydro cylinder piston. The string movement was converted into rotation via the fixed pulley block and rotating wheel, and it was output via the shaft. The signal conversion part was comprised of the bevel gear, worm, NdFeB magnet, and signal processer. The bevel gear and worm connected with the magnet to drive the magnet to rotate and produce a rotating magnetic field, which was detected by the signal processer and transferred into a voltage signal for the hydro cylinder control system.

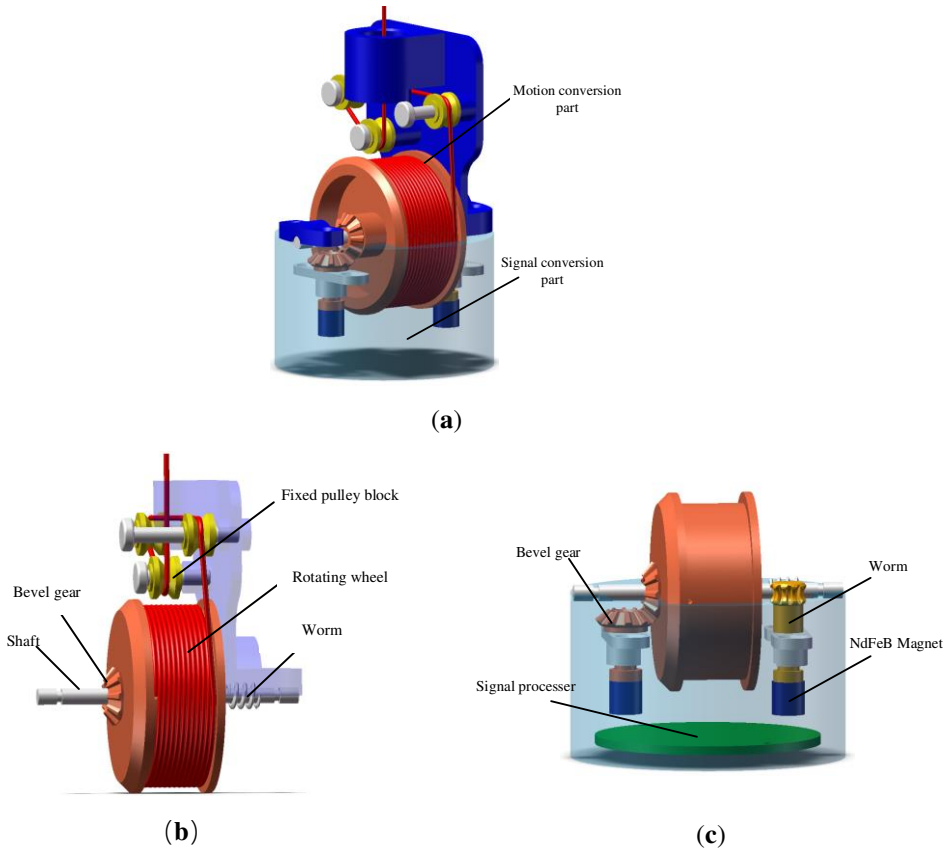

Figure 1. Structure of the proposed displacement sensor. (**a**) Overall structure. (**b**) Motion transformation part. (**c**) Signal transformation part.

2.2. Magnetic Field Analysis

Figure 2 shows the 3D FEM analyses. From these figures, the magnetic field distribution of the test point at the bottom of the magnet was sinusoidal.

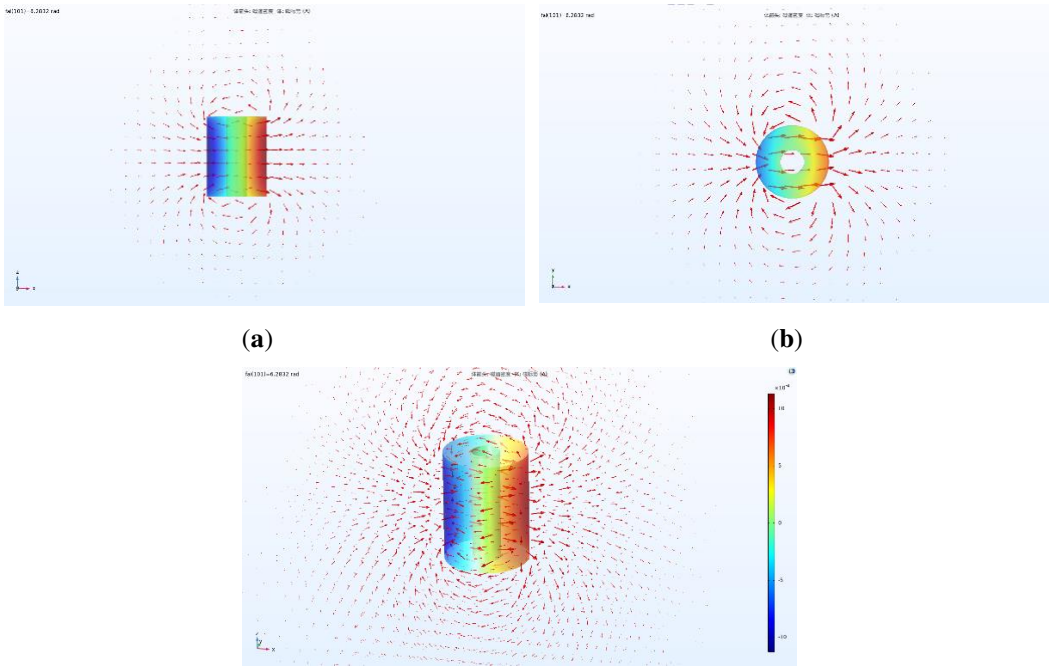

(**a**) (**b**)

(**c**)

Figure 2. Permanent magnet magnetic field distribution. (**a**) Side view. (**b**) Top view. (**c**) Overall distribution.

Figure 3 shows the variation of magnetic scalar potential at four points at the bottom of the magnet. The simulation result showed that when the magnet rotates the phase difference of magnetic induction intensity at the four points at the bottom of the magnet was 90 degrees.

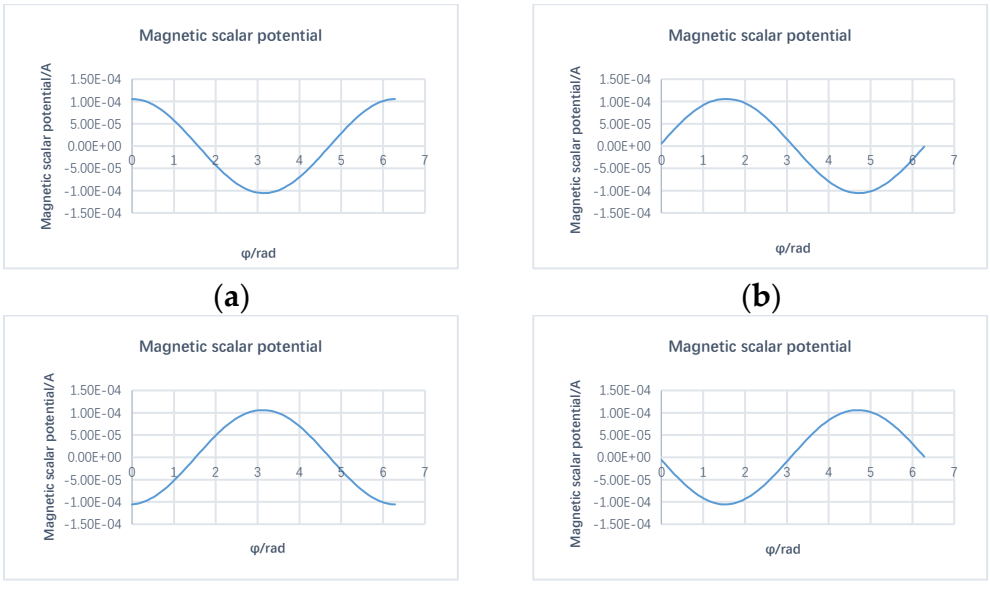

(**a**) (**b**)

(**c**) (**d**)

Figure 3. Variation of magnetic scalar potential at four points at the bottom of the magnet

2.3. Indirect Magnetic-to-Digital-to-Voltage Converter

Figure 4 shows a signal processor system block diagram. The proposed signal processor was composed of the magnetic field position sensor, MCU, voltage reference, 0-5 V voltage output, serial communication module, and power supply module. The magnetic field position sensor converted the rotating magnetic field signal shown in Figures 2 and 3 into an electrical signal and transmitted it to MCU. The MCU rotating magnetic field sensor data could obtain the accurate rope pulling length value via angle displacement conversion and filtering algorithm. The voltage reference support allowed for the voltage output module mapped the calculated length value to 0-5 V to provide information for sensor back-end devices.

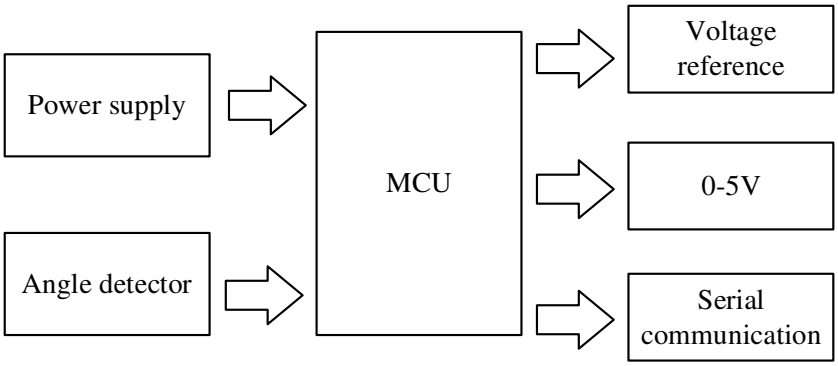

Figure 4. The diagram of the sensor hardware

Figure 5 shows a diagram of the angle position sensor system. The rotary position sensor was composed of a Hall sensor array, differential amplifier, ADC, digital filter, signal processing, and so on. The Hall sensor was located directly below the rotating magnetic field to detect the magnetic field component perpendicular to the surface. The four Hall sensors were distributed along the circumference with a phase difference of 90° and their centers were concentric with the rotating magnetic ring. The magnetic ring rotation allowed for the four Hall sensors to produce four orthogonal sinusoidal signals. Two orthogonal analog sinusoidal signals were obtained via differential amplification of signal 1 and signal 3, signal 2, and signal 4. After ADC conversion, digital filtering , and processing, the current angle value of the magnetic ring was obtained.

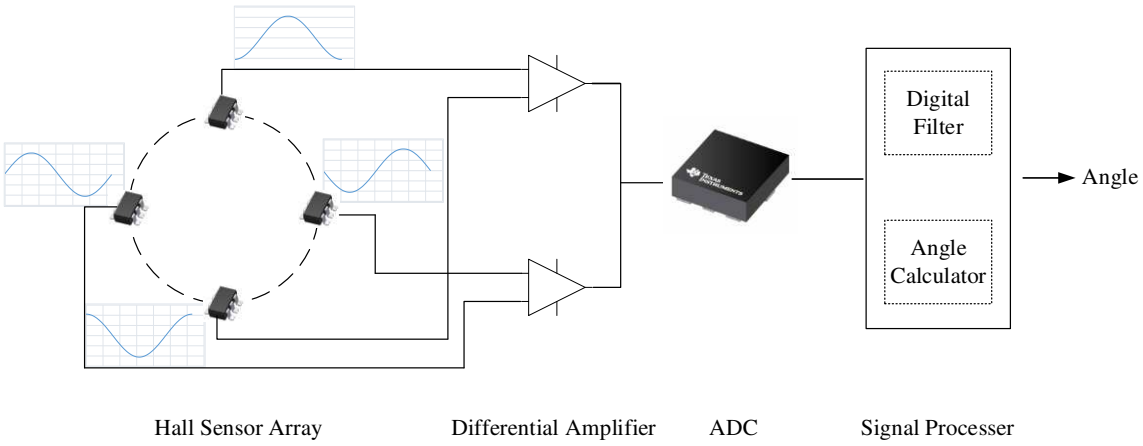

Figure 5. The diagram of the angle position detection module

3. Signal Processing Method Based on the Adaptive Kalman Filter

3.1 Method of Absolute Displacement Calculation Base on CORDIC

The Coordinate Rotation Digital Computer (CORDIC) algorithm was the coordinate digital rotation algorithm, which was an angle calculation method. The CORDIC algorithm included three rotating coordinate systems: circular, linear, and hyperbolic. Under each coordinate system, two working modes existed: rotation and vector. The CORDIC method core was to decompose θ into n decreasing rotation angles θ_i and add them.

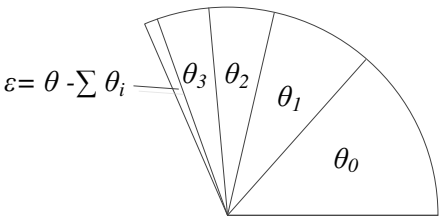

Figure 6. Principle of CORDIC

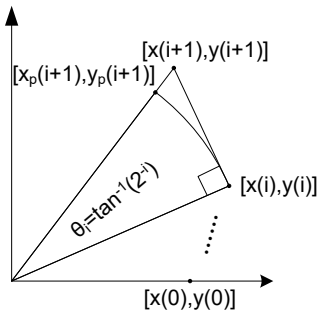

Figure 7. Iterative method of CORDIC

The basic CORDIC idea was to regard θ as a combination of a series of basic angles, and these basic angles satisfied the condition $\theta_i = \arctan(2^{-i})$. If the input vector was $\overrightarrow{V_{in}}$, after continuous rotation of the basic angle, the input vector

gradually approached the target vector $\overrightarrow{V_{out}}$. Figure 6 shows that if [x(i),y(i)] rotated the angle θ_i counterclockwise to obtain [xp(i+1),yp(i+1)], suppose:

$$\overrightarrow{\mathrm{V}_i} = (\cos\varphi, \sin\varphi) \tag{1}$$

$$\overrightarrow{\mathrm{V}_{i+1}} = (\cos(\varphi+\theta), \sin(\varphi+\theta)) \tag{2}$$

where l was the vector module length and φ was the vector rotation angle value. The relationship between the vector coordinates before and after rotation was:

$$\begin{bmatrix} x_{i+1} \\ y_{i+1} \end{bmatrix} = \begin{bmatrix} \cos\theta & -\sin\theta \\ \sin\theta & \cos\theta \end{bmatrix} \begin{bmatrix} x_i \\ y_i \end{bmatrix} \tag{3}$$

The formula of [x(i+1),y(i+1)] could be obtained by adding a gain of $1/cos\theta_i$ after each rotation:

$$x(i+1) = \frac{x_p(i+1)}{\cos\theta_i} = \frac{\cos\theta_i \cdot x(i) - \sin\theta_i \cdot y(i)}{\cos\theta_i} = x(i) - 2^{-i} \cdot y(i) \tag{4}$$

$$y(i+1) = \frac{y_p(i+1)}{\cos\theta_i} = \frac{\sin\theta_i \cdot x(i) + \cos\theta_i \cdot y(i)}{\cos\theta_i} = 2^{-i} \cdot x(i) + y(i) \tag{5}$$

After multiple iterations utilizing the CORDIC algorithm, the initial vector $\overrightarrow{V_{in}} = [1,0]$ was constantly approaching the target vector $\overrightarrow{V_{out}} = [cos\theta, sin\theta]$. After iterative tracking, the output of $x(i+1)$ and $y(i+1)$ was A times of the corresponding sine and cosine to the angle θ.

The CORDIC algorithm was applied to the magnet rotation angle calculation, the initial vector V0 was rotated a preset number of times, the angle value of each rotation process was calculated, and the current angle value of the magnet could be obtained via superposition.

The vector z was introduced to record the rotated angle value, and s_i was utilized as the rotation direction parameter. After m rotations, if y_m was greater than zero, it meant that the vector V_m was above the x-axis, and s_m was marked as -1, which meant that $m+1$ rotations were needed to follow the clockwise direction and angle; on the contrary, if y_m was less than zero, meaning that the vector V_m was below the x-axis, and s_m was marked as 1, which meant that $m+1$ rotations needed to be counterclockwise, $z_{m+1} = z_m + \theta_m$.

After multiple vector iterations, the output angle value approximated the target Angle θ. In other words, for the initial vector $\vec{V}_0 = (V_p \sin\theta, V_p \cos\theta)$, continuously rotated the angle so that the vector approached the X-axis. Because the

initial Angle Z_0 was 0, the accumulation of each iteration angle approximated the target angle[17].

$$x(i+1) = x(i) - s_i \cdot 2^{-1} \cdot y(i) \tag{6}$$

$$y(i+1) = s_i \cdot 2^{-1} \cdot x(i) + y(i) \tag{7}$$

$$z_{i+1} = z_i - s_i \cdot \arctan(2^{-i}) \tag{8}$$

$$s_i = \begin{cases} 1 & y_i < 0 \\ -1 & y_i > 0 \end{cases} \tag{9}$$

$$\begin{cases} \mathrm{A} = \sum_{i=0}^{\mathrm{n-1}} \cos\theta_i \\ \tan(\theta_i) = 2^{-i} \end{cases} \quad i = 1, 2, 3, ..., n \tag{10}$$

In the above, the preset angle was $\theta_i = \arctan(2^{-i})$, where $\sum_{i=0}^{\infty} \theta_i \to 90°$, which also meant that the rotation angle range was （$-90°$,$90°$）, but the rotation range of the encoder was 0~360°, so the range of operation angle needed to be extended.

For this reason, the angle interval was expanded by dividing the interval and setting the interval flag. The entire plane was divided into four quadrants according to the Cartesian coordinate system. When the vector was in the (+, +), (+, -) area, the input x and y values remained unchanged; when the vector was in the (-, +), (-, -) area, let $x' = -x, y' = -y$, the vector transferred into the first and fourth quadrants. After the CORDIC algorithm was executed, the angle value θ' was obtained, and the angle needed to be post-processed according to the flag bit value set in advance. For details, see the following table: θ' was the angle after the CORDIC algorithm, and θ was the final output angle after post-processing.

Table 1. Angle interval division

No.	Input	Coordinate transformation	Angle transformation
1	$(x \geq 0, y > 0)$	$x' = x,\ y' = y$	θ=θ′
2	$(x < 0, y \geq 0)$	$x' = -x,\ y' = -y$	θ=θ′+180°
3	$(x \leq 0, y < 0)$	$x' = -x,\ y' = -y$	θ=θ′+180°
4	$(x > 0, y \leq 0)$	$x' = x,\ y' = y$	θ=θ′+360°

Figure 2 shows that the two rotating magnetic fields were connected to the rotating wheel output shaft through a bevel gear and a worm gear. The bevel gear transmission ratio was 1:1, and the transmission ratio of the worm gear was 10:1. The CORDIC algorithm could be utilized to obtain the rotation angle of the two output shafts, and the displacement could be calculated via the following formula:

$$d = (\theta_1 + INT(k \times \theta_2)) \times r + d_0 \tag{11}$$

where d was the rope length calculated via the sensor，θ_1 was the magnet rotation angle attached to the bevel gear，θ_2 was the rotation angle of the magnet fixed to the worm gear，r was the rotating wheel radius， and d_0 was the initial state of the sensor.

3.2 Adaptive Kalman Filtering Based on Particle Swarm Optimization

Due to the presence of other interferences such as white noise, the position directly calculated via CORDIC was not accurate. An adaptive Kalman filter method was proposed to filter the calculation results.

A Kalman filter consisted of a prediction module and an error correction module. For a linear discrete system, the state space equation could be described as[18]:

$$\begin{cases} \mathbf{x}_{k+1} = \mathbf{A}_k \mathbf{x}_k + \mathbf{B}_k \mathbf{u}_k + \mathbf{\Gamma}_k \boldsymbol{\xi}_k \\ \mathbf{v}_k = \mathbf{C}_k \mathbf{x}_k + \mathbf{D}_k \mathbf{u}_k + \boldsymbol{\eta}_k \end{cases} \tag{12}$$

where A_k was the state transfer matrix, B_k was the input matrix, C_k was the observe matrix, u_k was the measurement noise sequence, and x_{k+1} was the real-time system state estimate.

For the displacement sensor system, assuming that the change value of the displacement with time has the first and second reciprocal, which each represented the speed and acceleration of the object, for small h values, the position and speed vectors $\boldsymbol{x}_k$ and $\dot{\boldsymbol{x}}_k$ satisfied the following equations:

$$\begin{cases} \mathbf{x}_{k+1} = \mathbf{x}_k + h\dot{\mathbf{x}}_k + \dfrac{1}{2}h^2\ddot{\mathbf{x}}_k \\ \dot{\mathbf{x}}_{k+1} = \dot{\mathbf{x}}_k + h\ddot{\mathbf{x}}_k \end{cases} \tag{13}$$

The observed value of the position acquired via the sensor was $\boldsymbol{v}_k = \boldsymbol{C}\boldsymbol{x}_k$, $\boldsymbol{C} = [1\ 0\ 0]$. The sensor tracking model could be expressed as the following equations:

$$\begin{cases} \begin{bmatrix} x_{k+1}[1] \\ x_{k+1}[2] \\ x_{k+1}[3] \end{bmatrix} = \begin{bmatrix} 1 & h & h^2/2 \\ 0 & 1 & h \\ 0 & 0 & 1 \end{bmatrix} \begin{bmatrix} x_k[1] \\ x_k[2] \\ x_k[3] \end{bmatrix} + \begin{bmatrix} \xi_k[1] \\ \xi_k[2] \\ \xi_k[3] \end{bmatrix} \\ v_k = \begin{bmatrix} 0 & 0 & 1 \end{bmatrix} \begin{bmatrix} x_k[1] \\ x_k[2] \\ x_k[3] \end{bmatrix} + \eta_k \end{cases} \tag{14}$$

Based on the above analysis, the Kalman filter was started from the initialization step[19]:

$$\hat{\mathbf{x}}_0 = E(\mathbf{x}_0) \tag{15}$$

$$\mathbf{P}_0 = E\left[(\mathbf{x}_0 - E(\mathbf{x}_0))(\mathbf{x}_0 - E(\mathbf{x}_0))^T\right] \tag{16}$$

Then the prediction process was conducted:

$$\hat{\mathbf{x}}_{k|k-1} = A\hat{\mathbf{x}}_{k-1} \tag{17}$$

$$\mathbf{P}_{k,k-1} = A\mathbf{P}_{k-1}A^T + \mathbf{\Gamma}_{k-1}\mathbf{Q}_{k-1}\mathbf{\Gamma}_{k-1}^T \tag{18}$$

The following step was the error correction process:

$$\hat{\mathbf{K}}_k = \hat{\mathbf{P}}_{k,k-1}C^T(C\hat{\mathbf{P}}_{k,k-1}C^T + R)^{-1} \tag{19}$$

$$\hat{\mathbf{x}}_k = \hat{\mathbf{x}}_{k|k-1} + K_k(\mathbf{v}_k - C\hat{\mathbf{x}}_{k|k-1}) \tag{20}$$

$$\mathbf{P}_k = (I - \hat{\mathbf{K}}_k C)\hat{\mathbf{P}}_{k,k-1} \tag{21}$$

The position of the sensor could be estimated via the above method. However, these ideal assumptions could not be satisfied due to various reasons. One of the most important reasons was that the exact statistical properties of the noise could not be obtained because the noise was produced via many reasons and could not be isolated directly from the measurement signals. Previous studies have shown that utilizing the wrong parameters of Q_k and R_k in the Kalman filter may degrade the performance of the state estimation. Therefore, the correct value of Q_k occupied a very important position in the Kalman filter.

An adaptive parameters optimization method based on particle swarm optimization (PSO) was proposed to reduce the parameter influence on the filter effect. In the proposed algorithm, the three-dimensional vector Q_k was set as the search space and the minimized displacement error was set as the search target. Suppose the population $X = \{x_1, \ldots x_i, \ldots x_m\}$ consisted of m particles, in which the position of the ith particle was $x_i = (x_{i1}, \ldots x_{i2}, \ldots x_{im})$, and its speed was $v_i = (v_{i1}, v_{i2}, \ldots v_{im})$. The individual extremum was $P_i = (p_{i1}, p_{i2}, \ldots p_{im})$ and the global population extremum was $P_g = (p_{g1}, p_{g2}, \ldots p_{gm})$. By following the principle of the current optimal particle, the particle X_i would change its speed and position via the following formula[20]:

$$v_i^{t+1} = v_i^t + c_1 r_1(p_i^t - x_i^t) + c_2 r_2(p_g^t - x_g^t) \tag{22}$$

$$x_i^{t+1} = x_i^t + v_i^{t+1} \tag{23}$$

where t was the number of iterations, c1 and c2 each represented the local accelerated constant and global accelerated constant, and r1 and r2 random numbers evenly distributed between 0 and 1.

Exploration meant that the particles leave the original optimization trajectory to a greater extent and entered a new direction to search; exploitation meant that particles continue the original optimization trajectory to a greater extent for detailed search. To better control the exploration and exploitation capabilities of the algorithm, an inertial weight w was introduced[21]:

$$v_i^{t+1} = w^t v_i^t + c_1 r_1 (p_i^t - x_i^t) + c_2 r_2 (p_g^t - x_g^t) \tag{24}$$

$$w^t = (w_{ini} - w_{end})(T_{\max} - t) / T_{\max} + w_{end} \tag{25}$$

where $T_{\max}$ was the maximum number of iterations, w_{ini} was the initial inertia weight, and w_{end} was the inertia weight in the maximum number of iterations. Utilizing linearly decreasing weight could expend the search space so that the global and local search capabilities of the algorithm could be adjusted for different search problems.

According to the above principles, when the displacement sensor works, the rotating magnetic field was obtained via the displacement detected module and transferred into the displacement of the object via the CORDIC algorithm. With the proposed adaptive Kalman filtering algorithm, the displacement and speed were updated in real-time and the measurement noise was filtered.

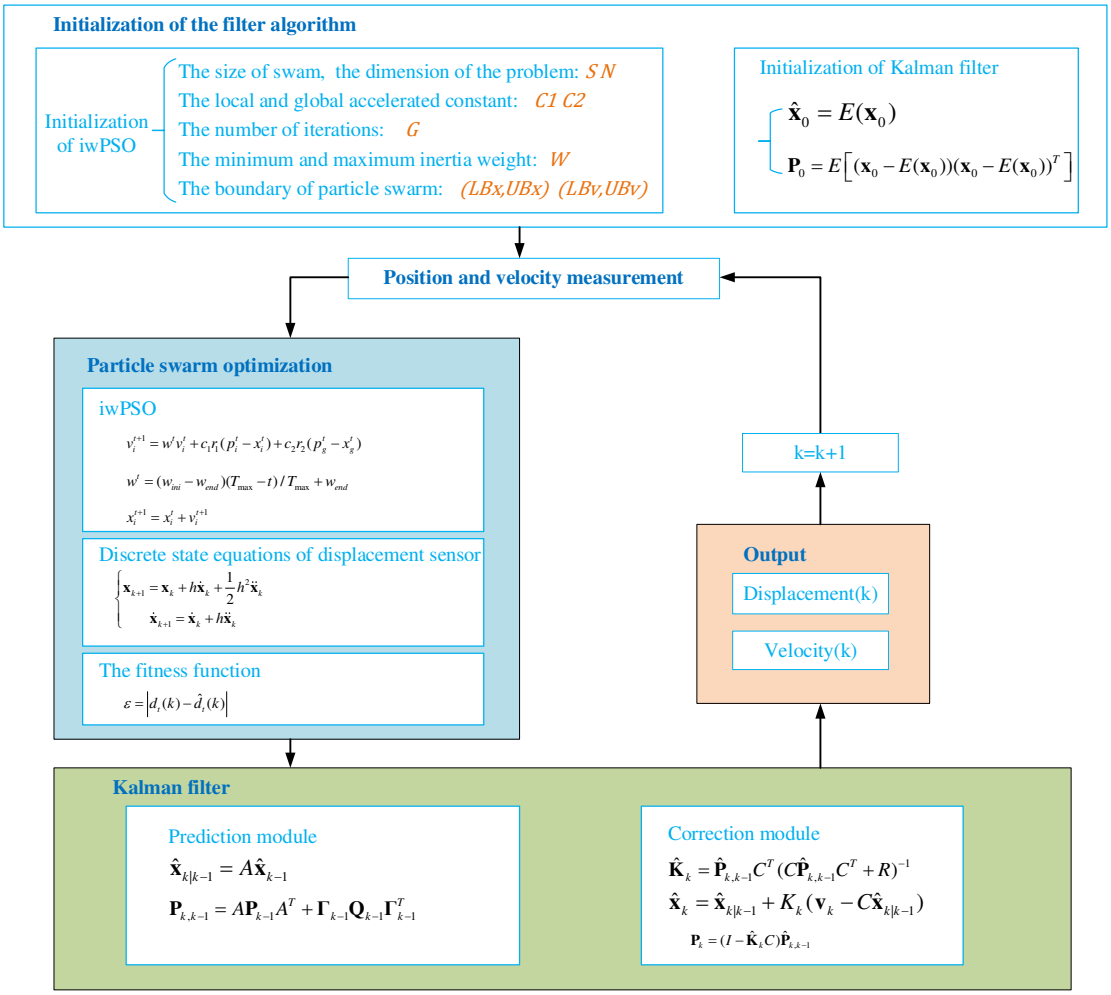

Figure 8. Schematic of the adaptive Kalman filtering

Figure 8. illustrates the steps of the proposed adaptive Kalman filtering algorithm:

1. Initialize the key parameters of the algorithm;
2. Obtain the displacement and speed via the displacement detected module and CORDIC algorithm;
3. Optimize the noise parameters Q_k and R_k in KF via the inertial weight PSO;
4. Based on the identified parameters, calculate the displacement and speed through KF;
5. Update the displacement and speed of the target object.

4. Experiments and Discussion

4.1 Experiments Configuration

Figure 9 shows the schematic diagram of the test bench. It consisted of four parts:

1. The sensor and the linear module. The linear module consisted of a motor (Panasonic A6 AC servo motor), a photoelectric encoder (23 bit), a motor driver. The sensor was fixed on

one end of the linear module, and the pull rope was fixed on the sliding platform of the linear module.

2. The power source (CHROMA 6205L, 60V-6A) and voltmeter (KEYSIGHT, 34465A). The power source supplies power for the sensor, the data transmission, and the linear module.
3. The data transmission module. The data transmission module generated the signal to control the motor and acquire the sensor data and transmit it to the data processer.
4. The signal and data processing tool, MATLAB R2019b unit in a host computer.

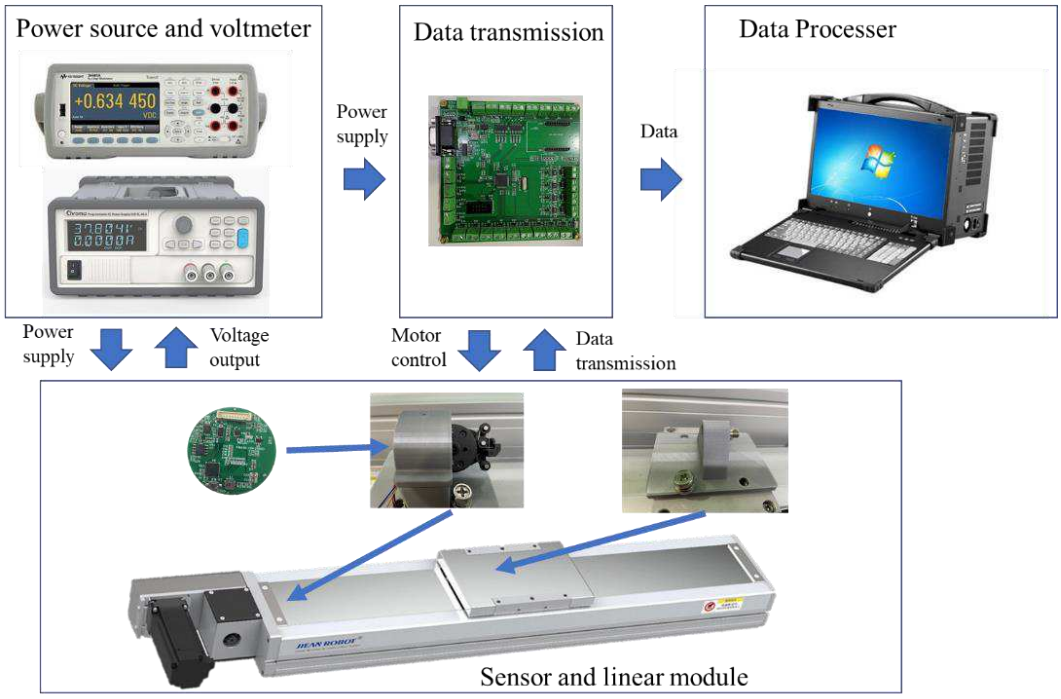

Figure 9. Schematic diagram of the sensor test bench

4.2 Displacement and Speed Estimate

Uniform linear motion was applied in the sensor to test the sensor accuracy and the AKF effect. The motor drove the linear module, and it pulled one end of the sensor to move linearly at a constant speed. The high precision photoelectric encoder provided the reference displacement during the platform moving. Figures 10 and 11 show that the maximum error of the sensor with CORDIC was 1.277 mm during the whole movement. The error came from two aspects: on the one hand, it was impossible to ensure that the magnet was installed directly above the angle detection; on the other hand, the calculation result was interfered via noise, such as the vibration of the linear module, from the environment. The maximum error of the sensor with the proposed AKF was 0.355 mm which was 27.8% of the error of the CORDIC.

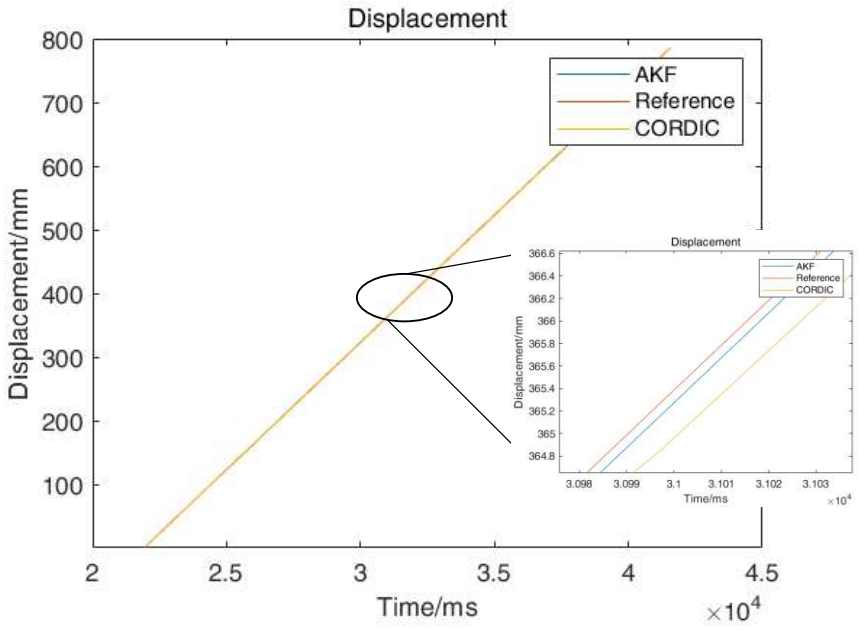

Figure 10. Sensor accuracy in uniform linear motion

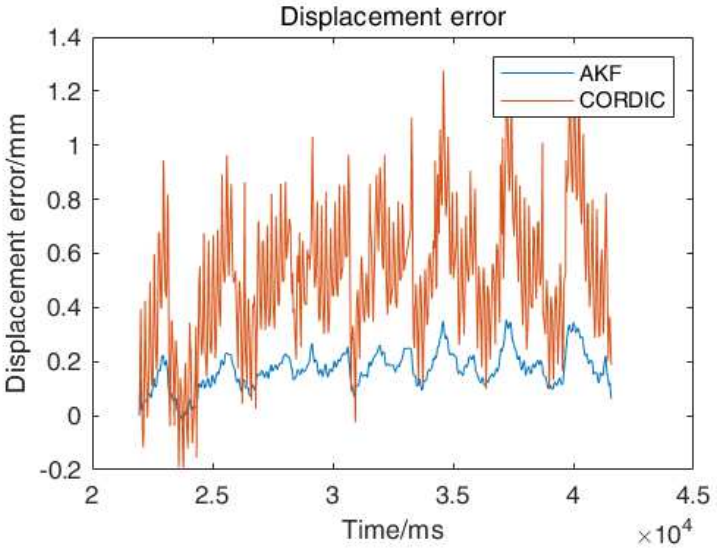

Figure 11. Displacement error of AKF and CORDIC

Figure 12 shows the speed and accelerated error of AKF and CORDIC.

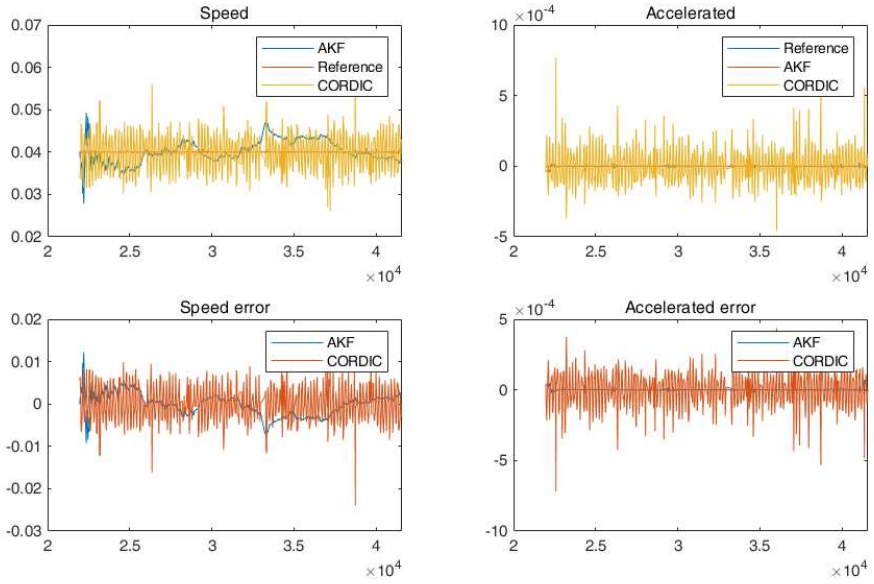

Figure 12. Speed and accelerated error of the proposed sensor

The maximum speed error of CORDIC was 0.0138 m/s and AKF was 0.0122 m/s. Because the object of PSO was displacement, the filtering effect of AKF for maximum speed error and the mean absolute error were not obvious. However, the maximum accelerated error of AKF was 0.000075 m/s^2 which was 17.4% of the CORDIC. Furthermore, the mean absolute error of AKF was only 3.2% of CORDIC. The proposed AFK could significantly improve the sensor accuracy.

Table 2. Sensor accuracy comparison

	Displacement Error		Speed Error		Accelerated Error	
	Max	**MAE**	**Max**	**MAE**	**Max**	**MAE**
CORDIC	1.277mm	0.5117	0.0138m/s	0.0036	0.00043	0.00011
AKF	0.3549mm	0.1692	0.0122m/s	0.0021	0.000075	0.0000036

5. Conclusions

The position measurement was greatly significant to industries, military, aerospace, and other fields. For underground equipment in coal mines, obtaining precise positions and postures of equipment could not only provided more information for equipment operators but also provided data support for the intelligent construction of coal mines. The present paper proposed a displacement sensor for measuring the telescopic stroke of the cylinder. A mechanical structure was proposed that can convert the displacement of the drawstring into a rotating magnetic field, and it calculated the angle value of the rotating magnetic field through the

CORDIC method. To solve the problem of measurement noise during sensor use, this paper proposed a Kalman filter method. An adaptive parameter optimization method based on PSO was proposed to solve the problem that the Kalman filter was sensitive to noise parameters. Experimental results showed that the position measurement accuracy of this sensor could reach 0.5 mm.

Author Contributions: Conceptualization, J.Z. and H.R.; methodology, Z.W.; software, S.G.; formal analysis, Z.H.; investigation, Z.W.; resources, H.R.; data curation, J.Z.; writing—original draft preparation, J.Z.; writing—review and editing, J.Z.; funding acquisition, H.R. All authors have read and agreed to the published version of the manuscript.

Funding: Please add: This work was supported by National Natural Science Foundation of China [grant numbers 51834006, 51804158] and National Key R&D Program of China for the 13th Five-Year Plan [grant number 2017YFC0603005].

Conflicts of Interest: The authors declare no conflict of interest.

References

[1] Cui, Y.; Wang, W.; Yang, M.; Gan, L.; Wang, Y., Development Trend and Status of the Servo Feedback Displacement Sensor. *Journal of Astronautic Metrology and Measurement* **2012,** 32, (4), 65-68.

[2] El Rawashdeh, Z.; Revel, P.; Prelle, C.; Letort, P.; Lamarque, F.; Ieee, *Fiber-Optic Sensor for Long Range Displacement Measurement of a Rotating Spindle*. 2016; p 248-253.

[3] Su, S.; Hou, Y.; Liu, W.; Zhang, H.; Liu, J., Review on fiber-optic displacement sensor. *Transducer and Microsystem Technology* **2015,** 34, (10), 1-3,7.

[4] Sandra, K. R.; Georg, B.; Kumar, J. V., Combined Variable Reluctance-Hall Effect Displacement Sensor. *Ieee Transactions on Instrumentation and Measurement* **2018,** 67, (5), 1169-1177.

[5] Sandra, K. R.; George, B.; Kumar, V. J., *A novel variable reluctance-hall effect transduction technique based displacement sensor*. 2017; p 5 pp.-5 pp.

[6] Popov, I. A., Eddy current displacement sensor. *Sensors and Systems* **2019**, (6), 26-30.

[7] Deng, D.; Wang, S.; Zheng, D., Eddy current pressure sensor based on planar coil. *Journal of Engineering-Joe* **2019,** 2019, (23), 8637-8640.

[8] Bertacchini, A.; Lasagni, M.; Sereni, G., *Ultra-Low Power Displacement Sensor*. 2020; p 251-7.

[9] Yang, H. Z.; Qiao, X. G.; Luo, D.; Lim, K. S.; Chong, W.; Harun, S. W., A review of recent developed and applications of plastic fiber optic displacement sensors. *Measurement* **2014,** 48, 333-345.

[10] Ferrazzin, D.; Di Domizio, G.; Salsedo, F.; Avizzano, C. A.; Tecchia, F.; Bergamasco, M.; Ieee, I., *Hall effect sensor-based linear transducer*. 1999; p 219-224.

[11] Bodnicki, M.; Pakula, P.; Zowade, M., Miniature displacement sensor. In *Advanced Mechatronics Solutions*, Jablonski, R.; Brezina, T., Eds. 2016; Vol. 393, pp 313-318.

[12] Wang, G.; Xu, Y.; Ren, H., Intelligent and ecological coal mining as well as clean utilization technology in China: Review and prospects. *International Journal of Mining Science and Technology* **2019,** 29, (2), 161-169.

[13] Guofa, W.; Yihui, P., Surrounding rock control theory and longwall mining technology innovation. *International Journal of Coal Science & Technology* **2017,** 4, (4), 301-9.

[14] Wang, B.-w.; Zhang, L.-y.; Wang, P.; Li, H.; Shi, R.-x.; Sun, Y.; Weng, L., Analysis of detection signal for magnetostrictive displacement sensor. *Optics and Precision Engineering* **2016,** 24, (2), 358-64.

[15] Chen, L.; Kim, Y.; Bae, Y., Long Range Displacement Measurements Systems Using Guided Wave. *International Journal of Fuzzy Logic and Intelligent Systems* **2017,** 17, (3), 154-161.

[16] Dai, Q.; Zhou, X., Modeling and Analysis of Elastic Wave of Large-Range Magnetostrictive Displacement Sensor. *Chinese Journal of Sensors and Actuators* **2013,** 26, (2), 195-9.

[17] Volder, J. E., The cordic trigonometric computing technique. *Institute of Radio Engineers Transactions on Electronic Computers* **1959,** EC-8, (3), 330-334.

[18] Houtekamer, P. L.; Zhang, F., Review of the Ensemble Kalman Filter for Atmospheric Data Assimilation. *Monthly Weather Review* **2016,** 144, (12), 4489-4532.

[19] Li, Q.; Li, R.; Ji, K.; Dai, W., *Kalman Filter and Its Application*. 2015; p 74-77.

[20] Bansal, J. C., Particle Swarm Optimization. In *Evolutionary and Swarm Intelligence Algorithms*, Bansal, J. C.; Singh, P. K.; Pal, N. R., Eds. 2019; Vol. 779, pp 11-23.

[21] Pant, S.; Kumar, A.; Ram, M., Reliability Optimization: A Particle Swarm Approach. In *Advances in Reliability and System Engineering*, Ram, M.; Davim, J. P., Eds. 2017; pp 163-187.

Figures

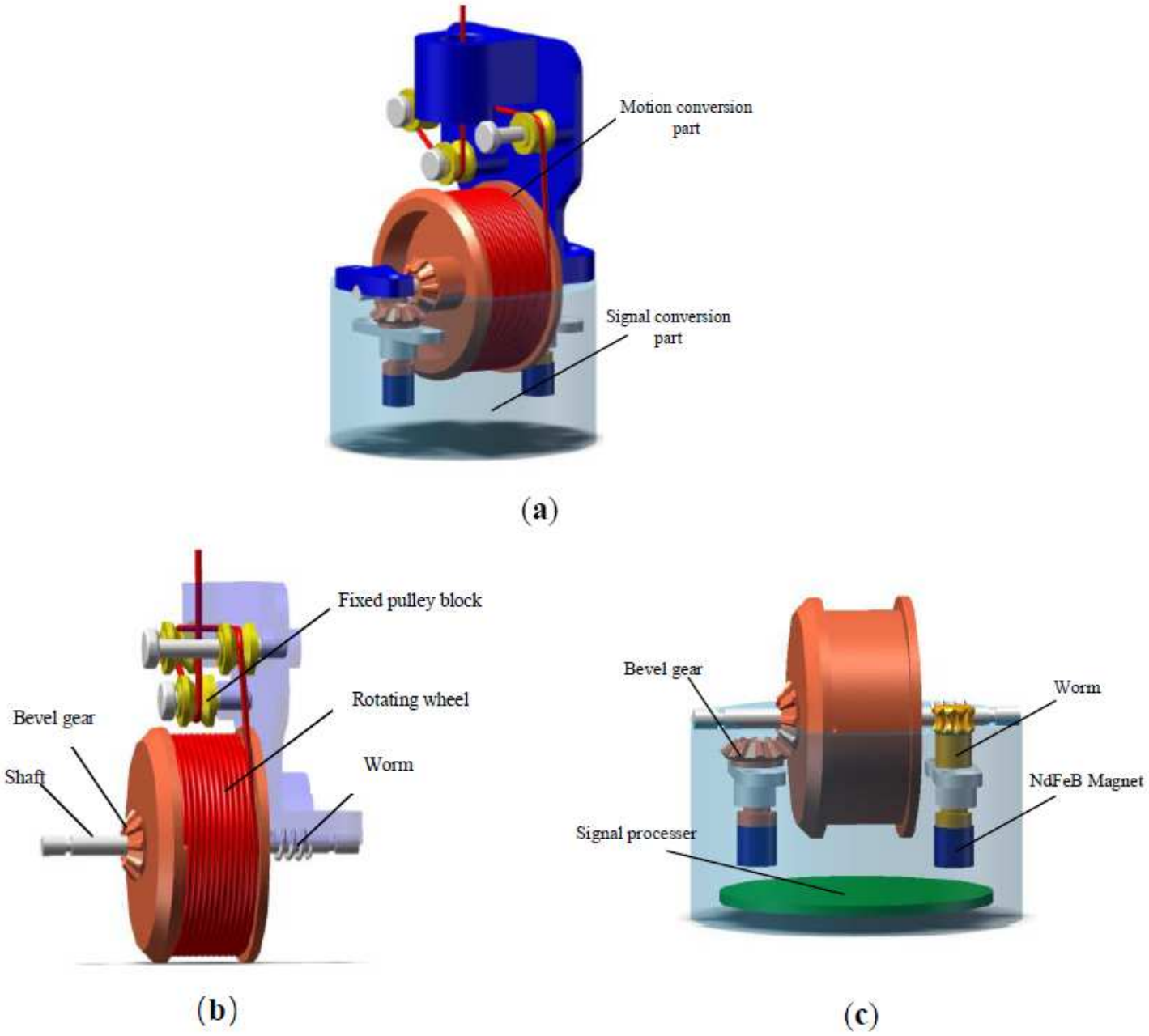

Figure 1

Structure of the proposed displacement sensor. (a) Overall structure. (b) Motion trans-formation part. (c) Signal transformation part.

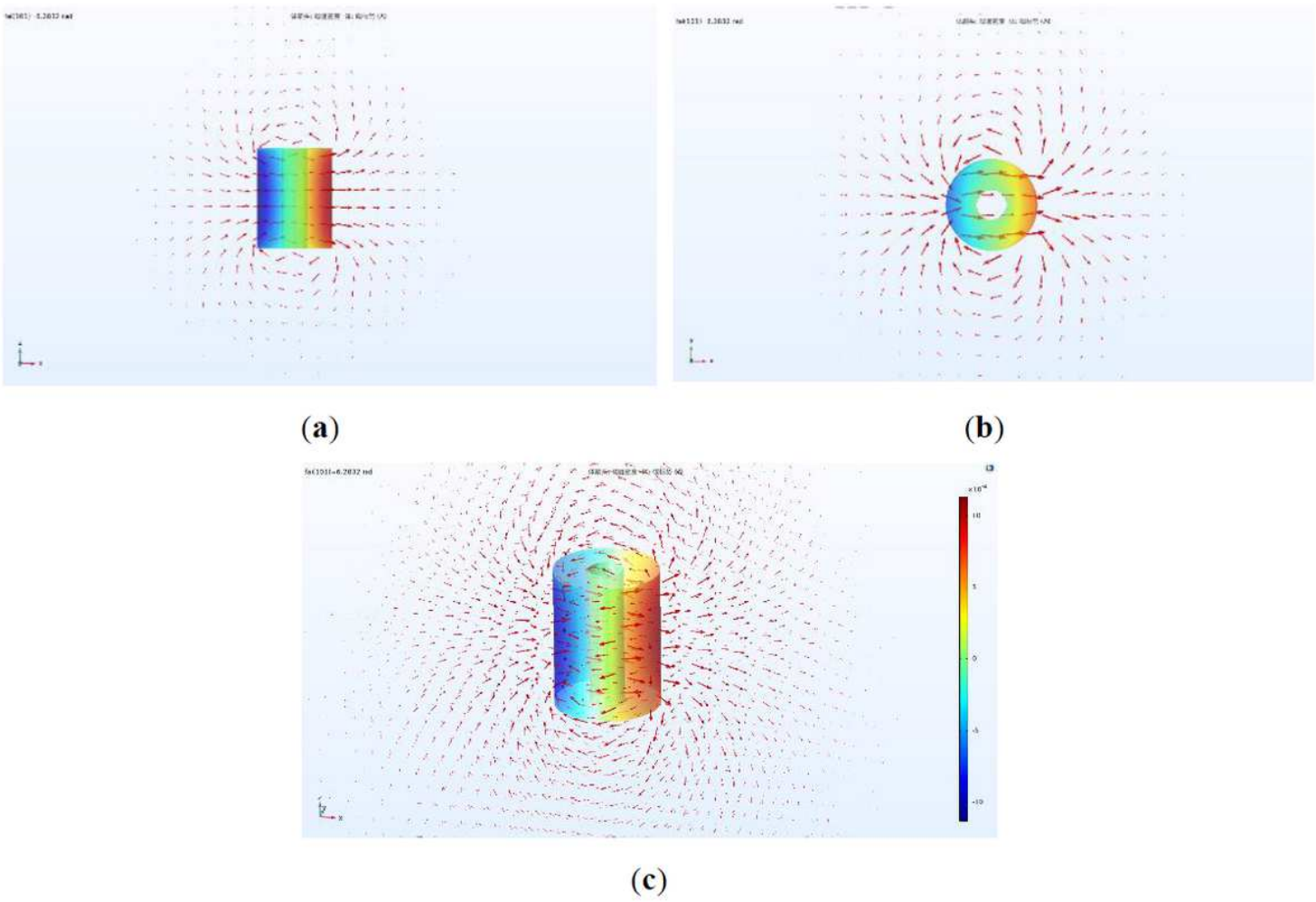

Figure 2

Permanent magnet magnetic field distribution. (a) Side view. (b) Top view. (c) Overall distribution.

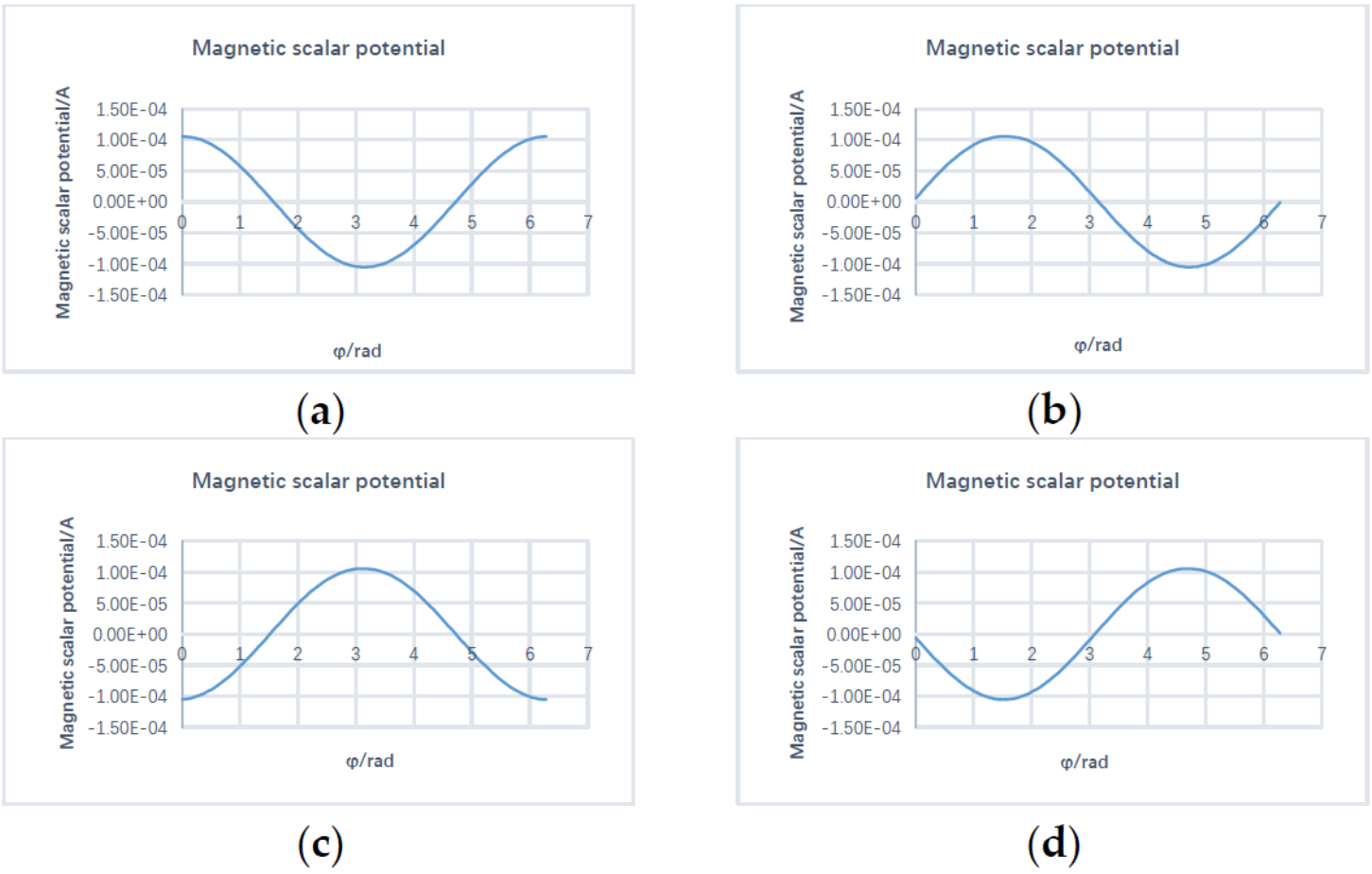

Figure 3

Variation of magnetic scalar potential at four points at the bottom of the magnet

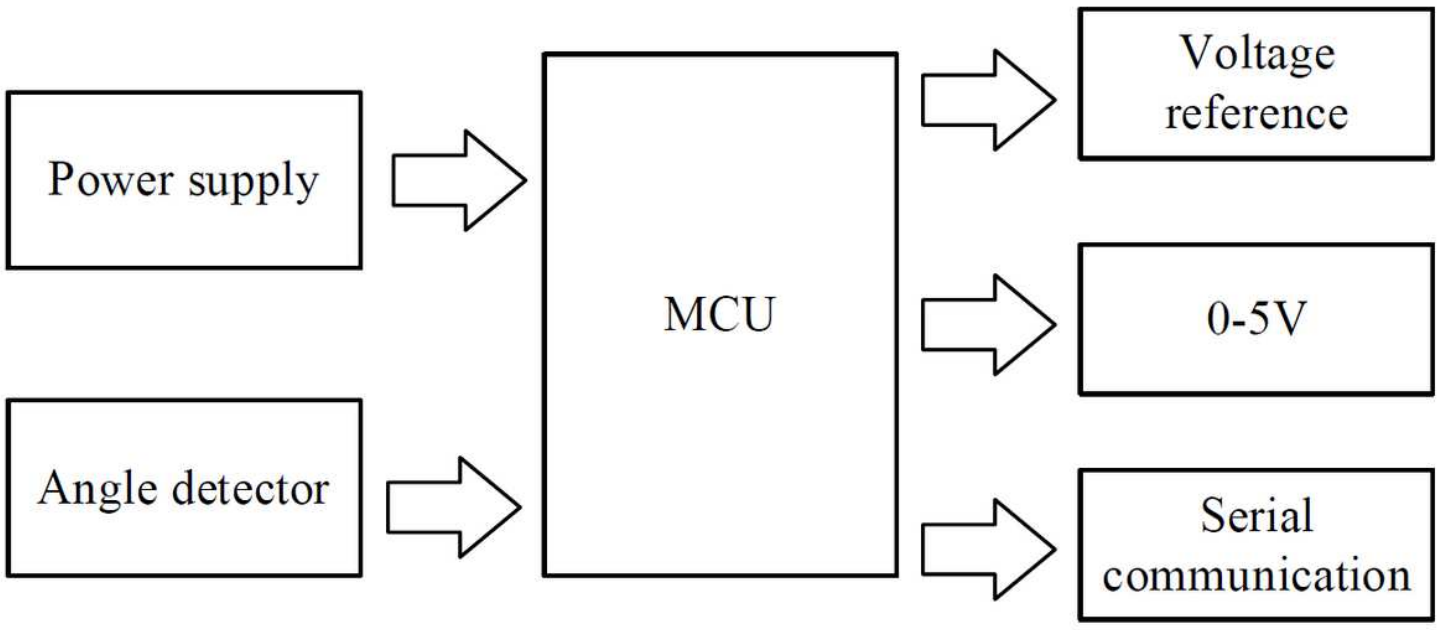

Figure 4

The diagram of the sensor hardware

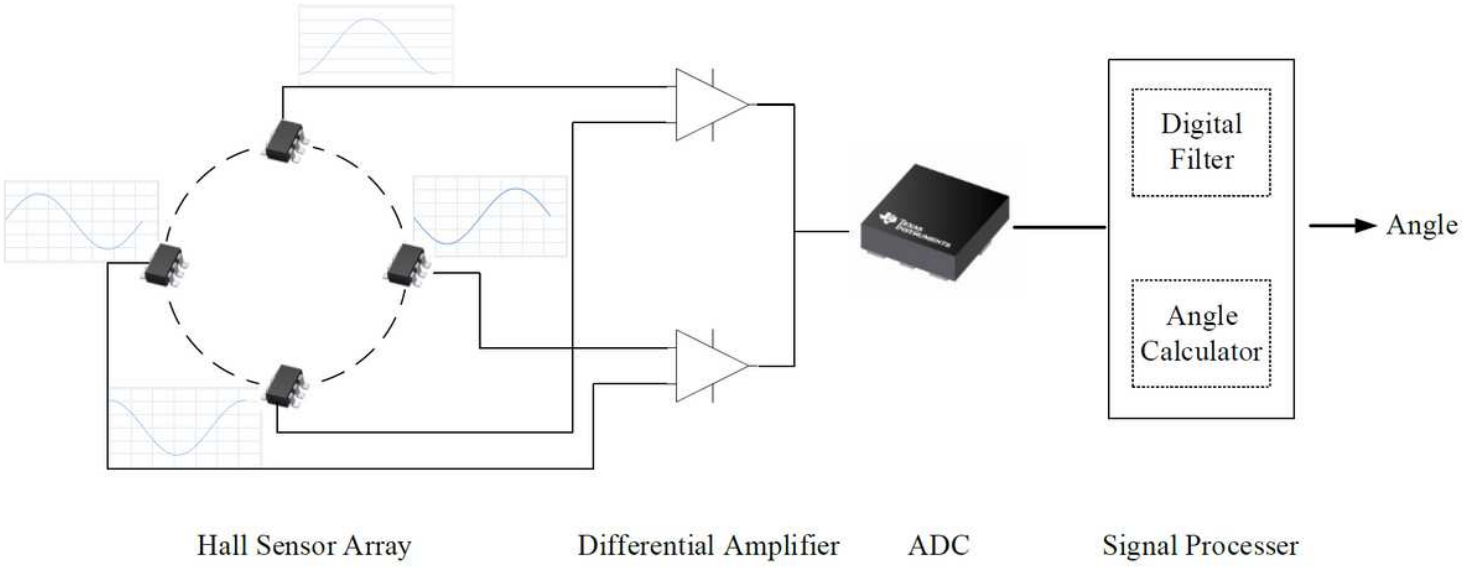

Figure 5

The diagram of the angle position detection module

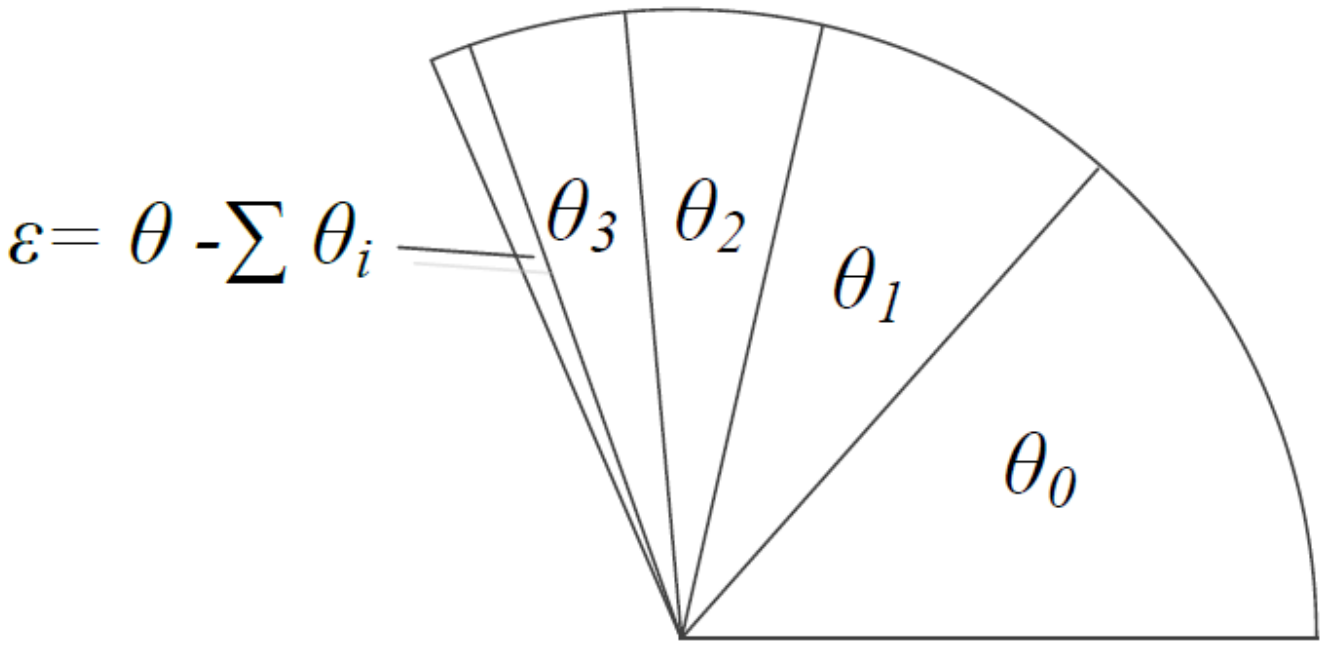

Figure 6

Principle of CORDIC

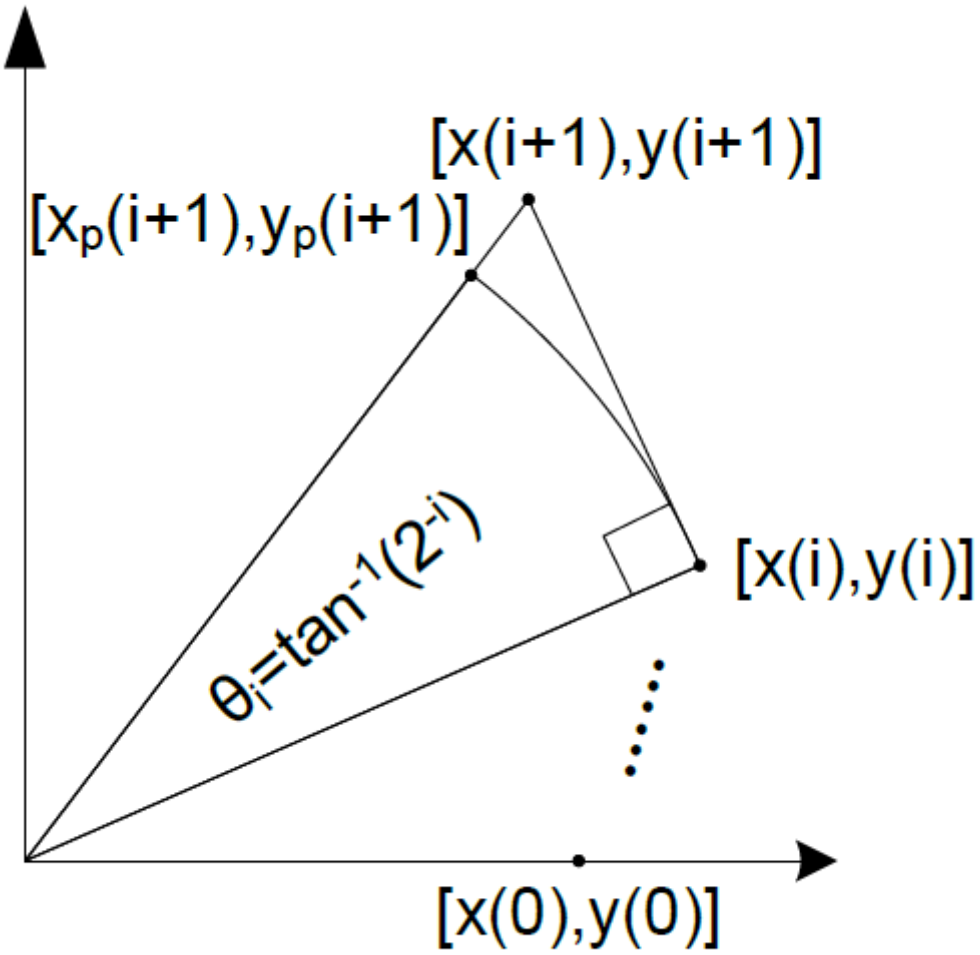

Figure 7

Iterative method of CORDIC

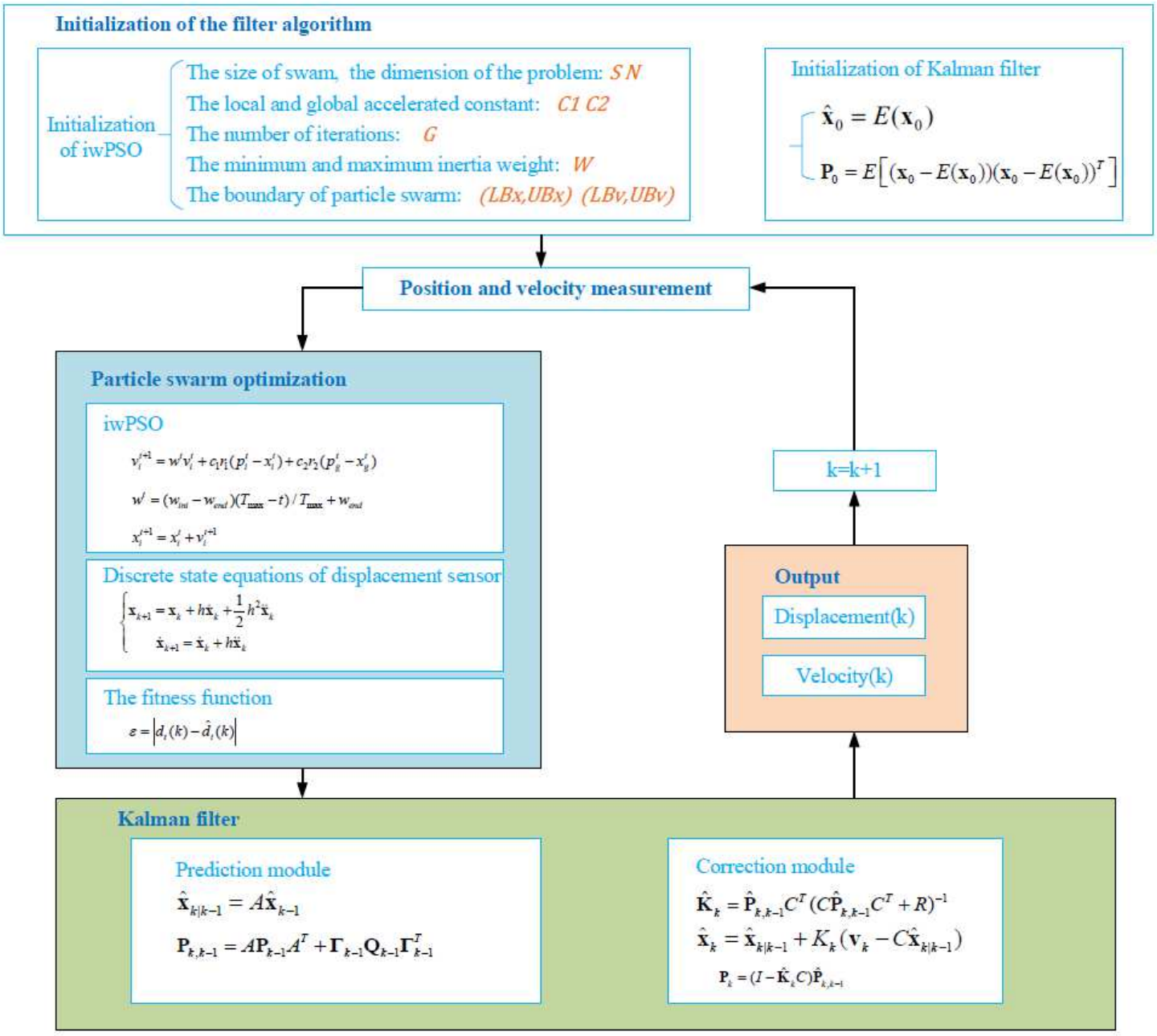

Figure 8

Schematic of the adaptive Kalman filtering

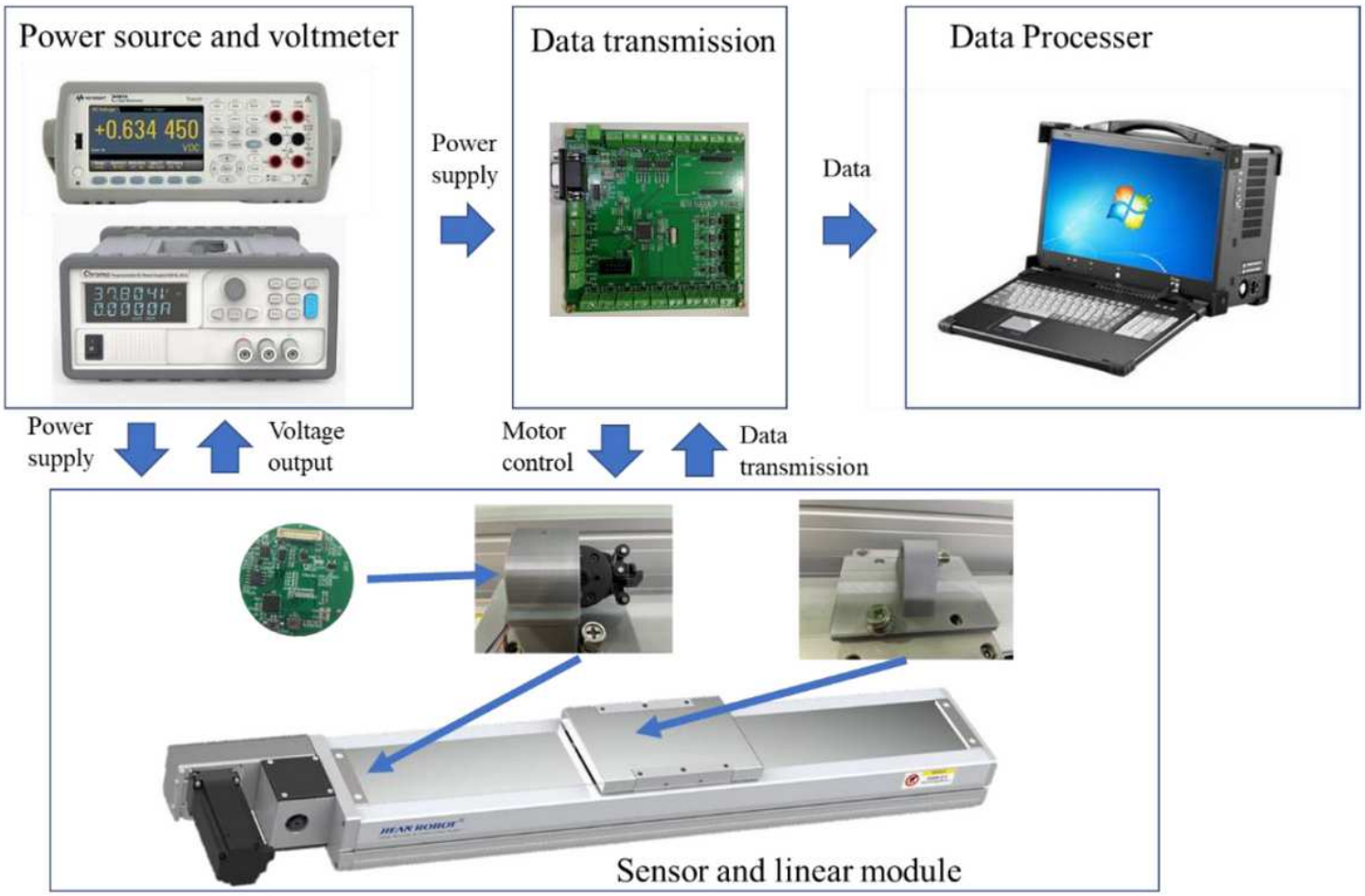

Figure 9

Schematic diagram of the sensor test bench

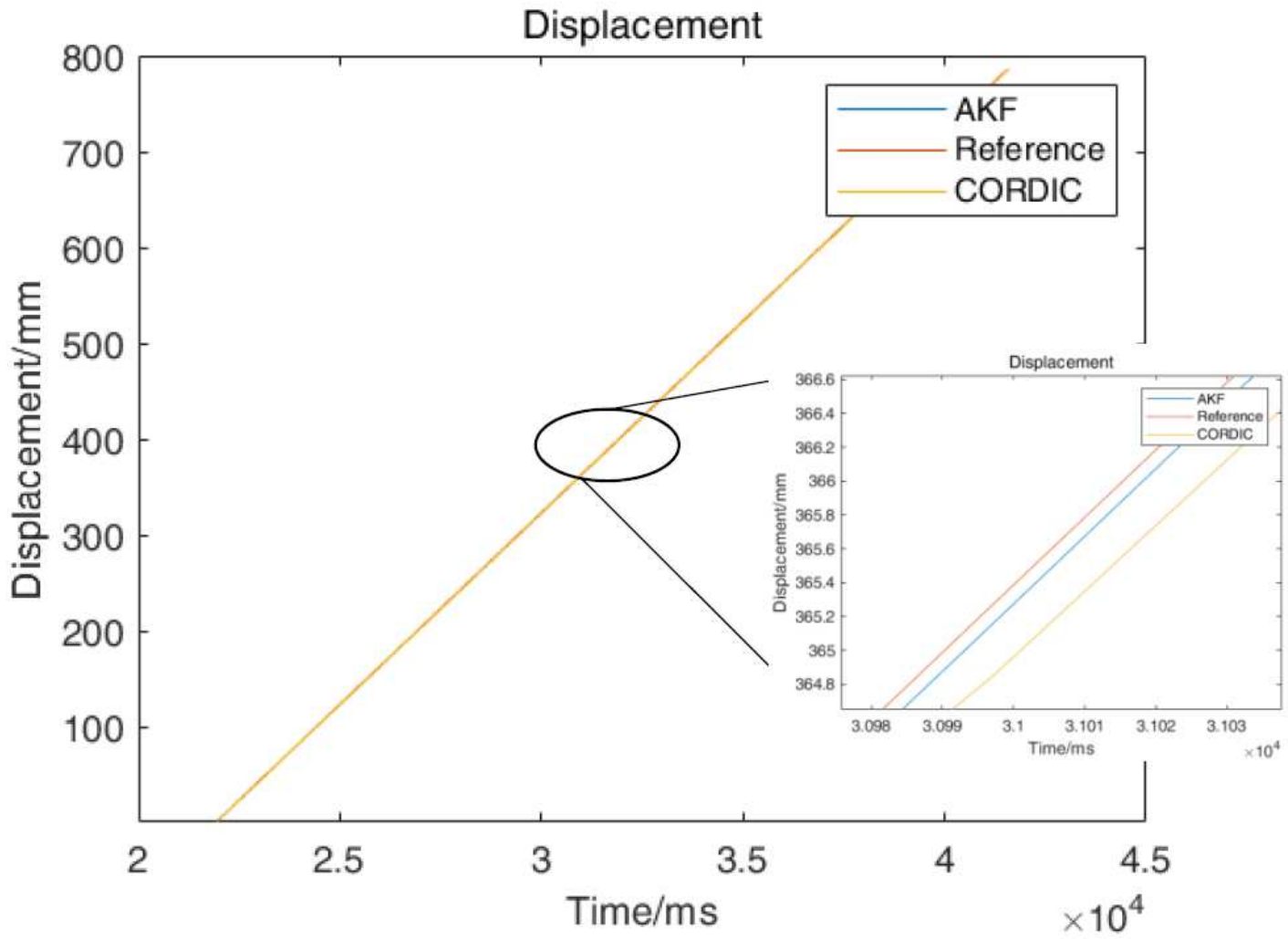

Figure 10

Sensor accuracy in uniform linear motion

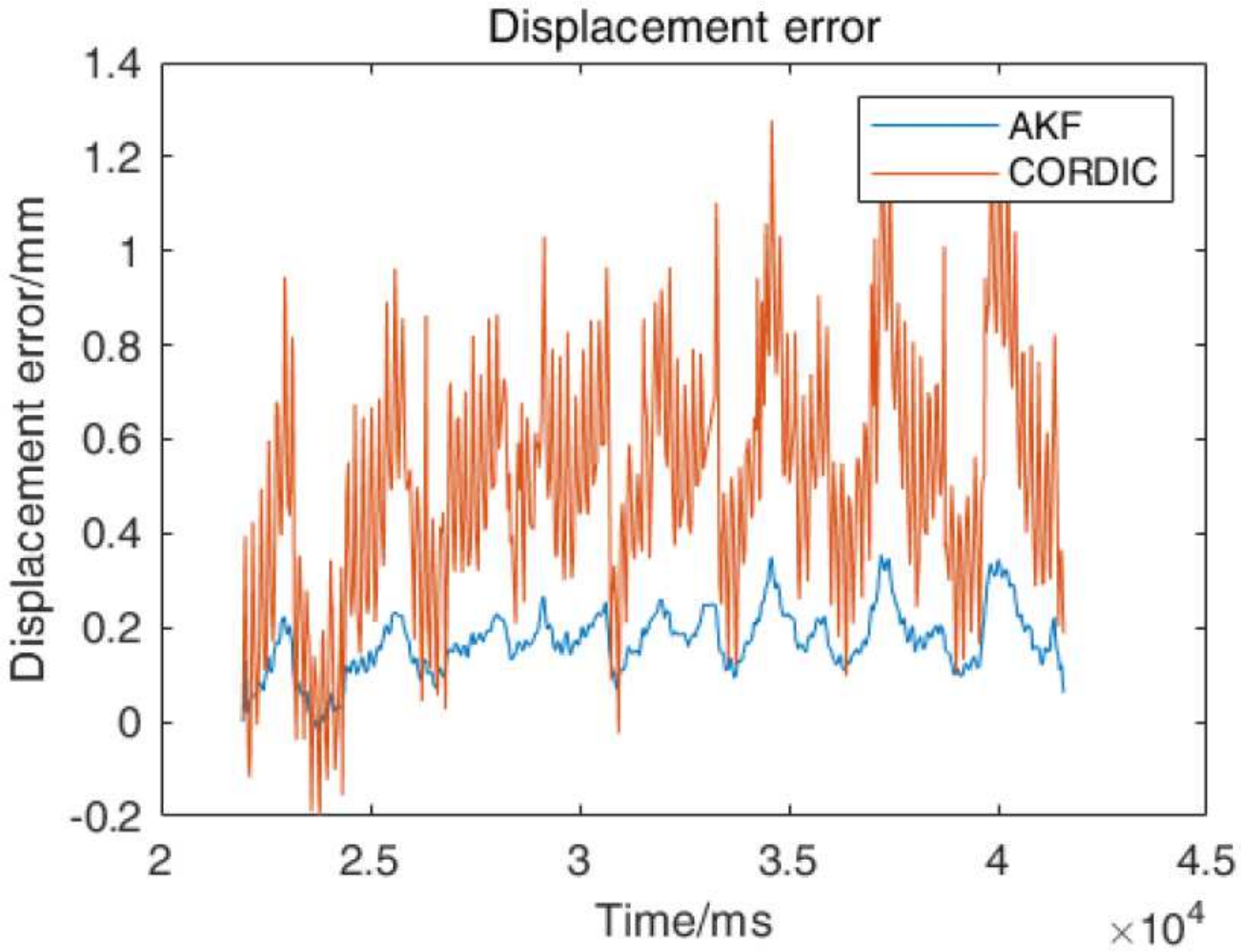

Figure 11

Displacement error of AKF and CORDIC

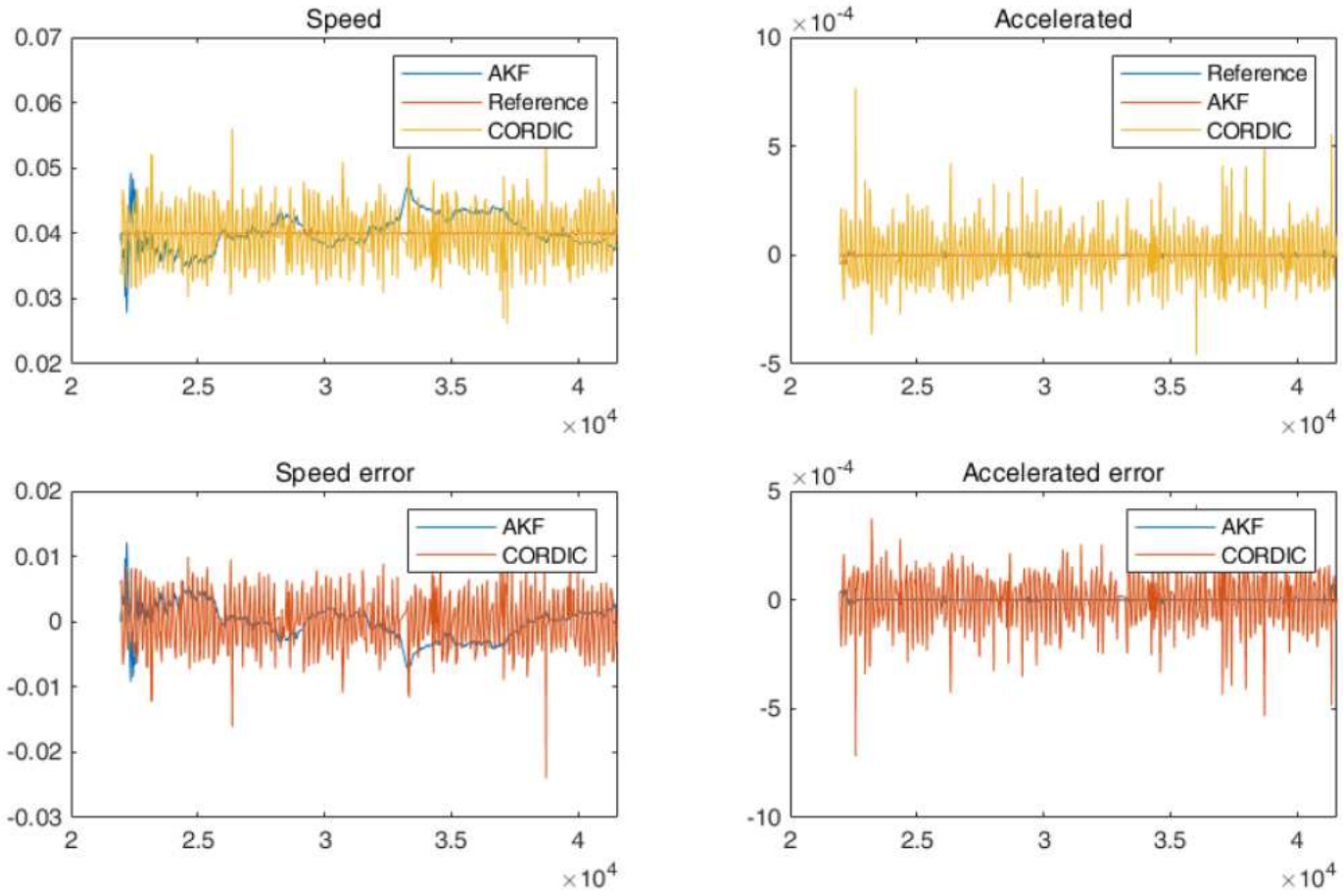

Figure 12

Speed and accelerated error of the proposed sensor